Low-melting-point alloys integrated extrusion additive manufacturing

Jingchao Jiang [1], Xiaoya Zhai [2], Kang Zhang [2], Liuchao Jin [2], Qitao Lu [2], Zhichao Shen [2], and Wei-Hsin Liao [2]

[1]The Chinese University of Hong Kong
[2]Affiliation not available

October 30, 2023

Abstract

Additive manufacturing has developed significantly. In contrast to established fabricated materials, low-melting-point alloys (LMPAs) are increasingly attractive because they have favorable electrical/thermal conductivities and mechanical strengths. However, LMPA additive manufacturing is still in its infancy. We report a novel strategy for fabricating the complex and/or multifunctional components of LMPAs by extrusion additive manufacturing with two nozzles (for extruding the polymer and for extruding the LMPA). The proposed strategy was used to successfully fabricate complex LMPA components for the first time. We fabricated LMPA/polymer composite parts with improved mechanical properties, and implemented the integrated manufacturing of circuits and 3D products. The strategy will enable the use of LMPAs in applications such as smart structures, electromagnetic shielding, biomedicine, thermal management, energy harvesting, and advanced electronics.

Low-melting-point alloys integrated extrusion additive manufacturing

*Jingchao Jiang[1]†, Xiaoya Zhai[1,2]†, Kang Zhang[1,3]†, Liuchao Jin[1], Qitao Lu[1], Zhichao Shen[1], Wei-Hsin Liao[1]**

[1]Department of Mechanical and Automation Engineering, The Chinese University of Hong Kong; Hong Kong, China.

[2]School of Mathematical Sciences, University of Science and Technology of China; Hefei, China.

[3]Nano and Advanced Materials Institute Ltd; Hong Kong Science Park, Hong Kong, China.

**Corresponding author. Email: whliao@cuhk.edu.hk.*

†These authors contributed equally to this work.

Abstract: Additive manufacturing has developed significantly. In contrast to established fabricated materials, low-melting-point alloys (LMPAs) are increasingly attractive because they have favorable electrical/thermal conductivities and mechanical strengths. However, LMPA additive manufacturing is still in its infancy. We report a novel strategy for fabricating the complex and/or multifunctional components of LMPAs by extrusion additive manufacturing with two nozzles (for extruding the polymer and for extruding the LMPA). The proposed strategy was used to successfully fabricate complex LMPA components for the first time. We fabricated LMPA/polymer composite parts with improved mechanical properties, and implemented the integrated manufacturing of circuits and 3D products. The strategy will enable the use of LMPAs in applications such as smart structures, electromagnetic shielding, biomedicine, thermal management, energy harvesting, and advanced electronics.

Keywords: additive manufacturing; 3D printing; low-melting-point alloy.

1. Introduction

Additive manufacturing (AM; also known as 3D printing) is a technique for fabricating parts in a point-by-point and then layer-by-layer manner from 3D model data.[1] Since the first AM technique was devised in the 1980s,[2] the applicability of various materials with regard to the method has been researched. These materials include metamaterials,[3] photopolymers,[4,5] ceramics,[6–8] cement,[9] metal,[10–14] and silica glass.[15] Low-melting-point alloys (LMPAs) are becoming increasingly attractive because they have certain advantages including favorable thermal conductivity, ease of handling, reusability, mechanical strength, and good electrical conductivity. LMPAs allow a metal to form into a liquid or semiliquid state at low temperatures (below 300°C at atmospheric pressure), and then resolidify.[16] An LMPA is usually composed of low-melting-point elements such as indium (In), gallium (Ga), tin (Sn), or bismuth (Bi).[17] LMPAs have already been widely used in bionics,[18,19] thermal management,[20,21] clean energy,[22] electromagnetic shielding,[23] and biomedicine.[24] Some researchers have already tried 3D printing LMPAs. Huang et al. (2022) used electric field-assisted direct writing to 3D print an LMPA.[25] It is possible to use their method to fabricate LMPA parts. However, the products suffer from low surface quality and low bonding strength between layers. Warrier and Kate (2018) used fused deposition modeling (FDM) to print pure LMPA parts directly.[26] However, the quality was relatively low and it was impossible to fabricate complex structures. Hsieh et al. (2016) also used FDM to directly manufacture an LMPA, although only three single layers were printed.[27] The literature shows that LMPAs have excellent potential for future multi-functional applications.[28–32] However, the fabrication of good quality complex LMPA parts by 3D printing techniques remains challenging, and additive manufacturing LMPA is still in its infancy.

Herein, we propose a novel extrusion additive manufacturing (EAM) strategy for fabricating complex LMPA parts with multi-functional applications at relatively low cost. The main idea is to use two nozzles during EAM: one for extruding the polymers (e.g., polylactic acid (PLA)) and another for injecting the LMPA. Figure 1(a) shows how the proposed system works. As shown step-by-step from left to right in this figure, when printing the polymer part of the component, nozzle 1 is open for fabrication. When the polymer part is completed, nozzle 2 opens to inject the molten LMPA. Once the whole component cools to below the melting temperature of LMPA, the molten LMPA solidifies, and the entire component is finished. The strategy proposed in the present paper has three novel aspects. First, for the first time it enables the fabrication of complex pure LMPA parts using EAM (a low-cost AM technique, compared with traditional metal AM). We printed various triply periodic minimal surface (TPMS)-based structures and lattice structures as examples. Second, the proposed system enables the fabrication of composite (polymer and LMPA) parts with improved mechanical properties. We printed standard parts for tensile and three-point bending tests. Third, the proposed system can be used to fabricate 3D products with internal LMPAs that act as electrical wires, thereby eliminating the necessity of further steps to insert the wires. We manufactured two test pieces to demonstrate this capability of the technique: a test piece comprising the letters CUHK (which stand for Chinese University of Hong Kong); and a test piece comprising a "spring light" (i.e., a light-emitting diode (LED) attached to a plastic spring with an internally printed LMPA that acts as an electrical wire). Figure 1(b) lists the potential applications of the strategy proposed herein.

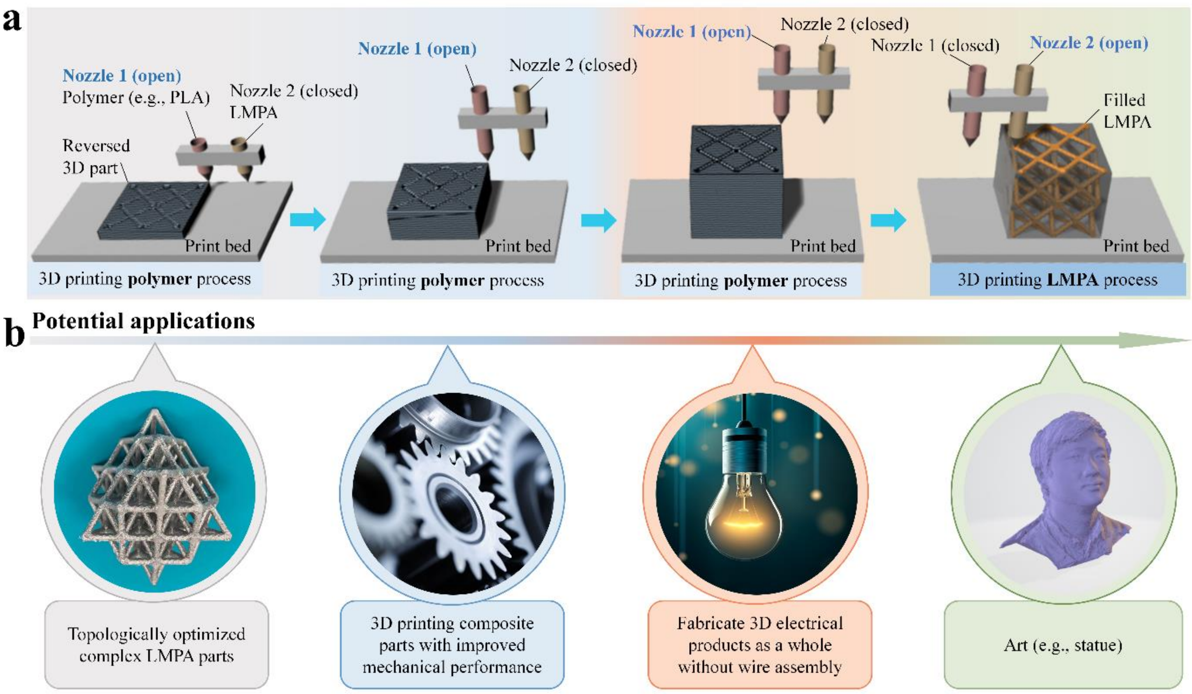

Figure 1. (a) Schematic showing the proposed printing system; (b) Potential applications.

2. Results and discussion

2.1. 3D printing of complex pure LMPA parts

The proposed strategy can be used for the 3D printing of complex pure LMPA parts. The process is illustrated in Figure 2(a). The final complex 3D part is designed first. The 3D part is then reversed using a bounding box to obtain the reversed 3D model. Next, the reversed 3D part is 3D printed using nozzle 1 (PLA) and the LMPA is filled inside the reversed 3D part using nozzle 2 to obtain the PLA/LMPA composite part. The composite part is then soaked in CH_2Cl_2 to dissolve the PLA and produce the complex pure LMPA part. Figure 2(b) shows several designed and fabricated complex pure LMPA parts, including various lattice, tooth, and bone structures. The details of these structure designs can be found in the supplementary information. Figure 2(c) shows a scanned 3D model of the first author's head and an LMPA statue fabricated from it. As indicated in the literature, LMPA has excellent potential for future multi-functional applications,[28–32] including smart structures, electromagnetic shielding, biomedicine, thermal management, and energy harvesting. To the best of our knowledge, our study is the first to demonstrate the fabrication of complex lattice, tooth, and bone LMPA structures using EAM, which is a low-cost AM technique. The ability to fabricate complex parts will facilitate the design of LMPA structures that can be applied with improved efficiency to more fields.

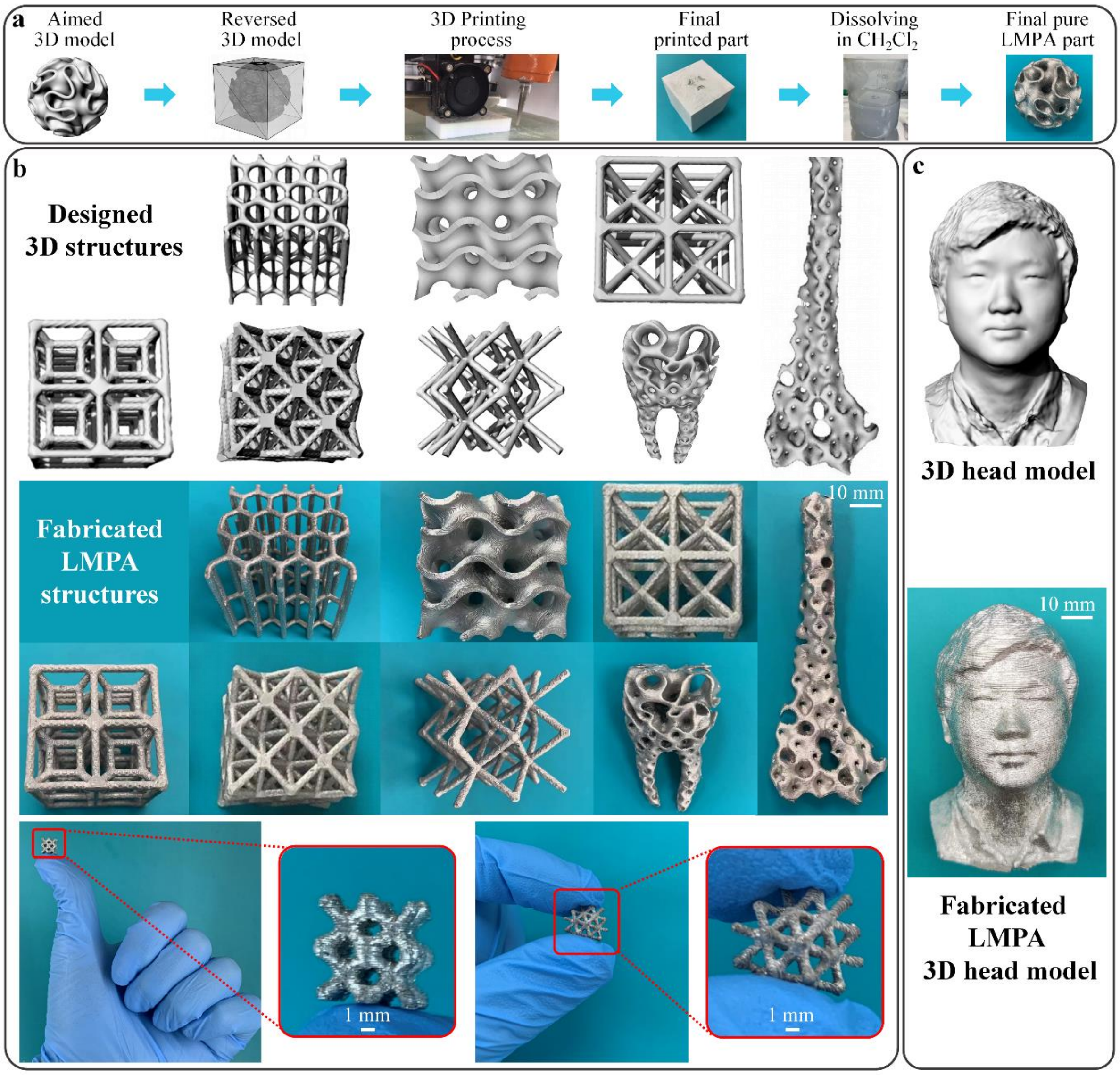

Figure 2. (a) Process by which the final pure LMPA parts are obtained; (b) Demonstration of printed complex pure LMPA parts; (c) Demonstration of a printed LMPA statue. (LMPA = low-melting-point alloy).

2.2 3D printing of composite parts

The fabricated parts of LMPA/polymer composites have better mechanical properties than traditional pure polymer 3D printed parts. The standard parts were designed for tensile and three-point bending tests. The details of the design are provided in the supplementary information. Both tensile and three-point bending tests were carried out three times in each condition (three parts printed for each design). Figure 3(a) shows the 3D printed pure PLA and PLA/LMPA standard parts used in the tensile tests. Figure 3(b) illustrates the tensile machine setup. Figure 3(c) shows the broken parts after the tests. Figure 3(d), (e), and (f) show the stress–strain curves of the PLA and PLA/LMPA parts subjected to testing speeds of 1, 50, and 100 mm/min, respectively. The Young's modulus and tensile strength values are also given in Figure 3(g). Both the Young's modulus and tensile strength of the PLA/LMPA composite part were much higher than those of the pure PLA part under the various testing conditions. When the testing speed was 50 mm/min, the tensile strength of the PLA/LMPA part was more than twice that of the pure PLA part. Figure 3(h) shows the 3D printed pure PLA and PLA/LMPA standard parts used in the three-point bending tests. Figure 3(i) shows the three-point bending machine setup. Figure 3(j) shows the broken parts after the tests. Figure 3(k), (l), and (m) show the load–displacement curves of the PLA and PLA/LMPA parts subjected to testing speeds of 1, 50, and 100 mm/min, respectively. The flexural modulus and flexural strength values are also shown in Figure 3(n). Both the flexural modulus and flexural strength of the PLA/LMPA composite part were much higher than those of the pure PLA part under the various testing conditions. When the testing speed was 100 mm/min, the flexural strength of the PLA/LMPA part was more than twice that of the pure PLA part. Figure 4 shows scanning electron microscopy (SEM) images of the fractured surfaces of the PLA and PLA/LMPA parts after the three-point bending and tensile tests under various conditions. In general, the fracture surfaces of the PLA parts were similar, regardless of the testing speed. However, the roughness of the fracture surfaces of the PLA/LMPA parts did vary significantly with the testing speed. As shown in Figure 4(a) and (d), at low testing speeds the facture surfaces appeared to contain several voids and were very rough. The voids gradually diminished, and the fracture surfaces became smoother (Figure 4(b)-(c) and Figure 4(e)-(f)) as the testing speed increased.

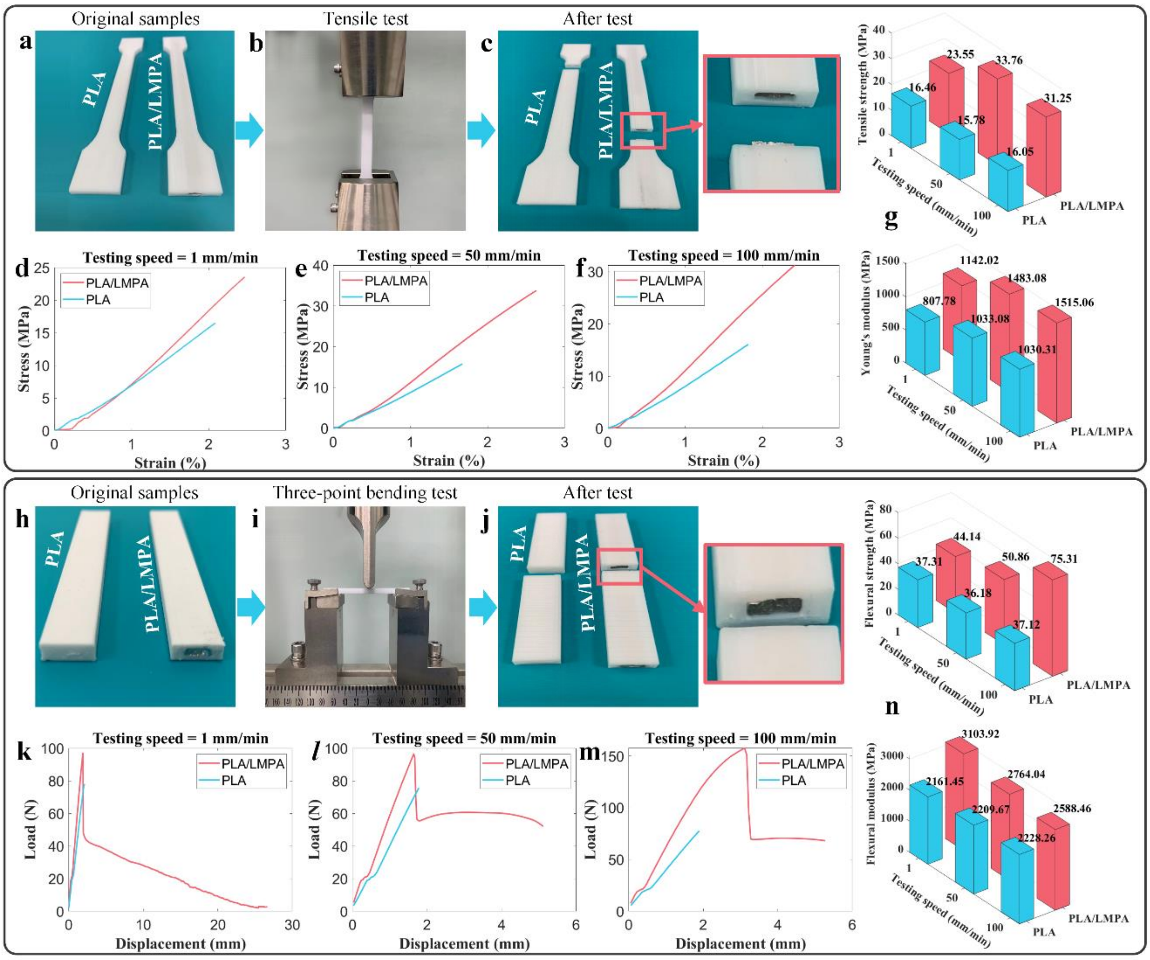

Figure 3. Tensile and three-point bending tests, and the corresponding results. (a) 3D printed PLA and PLA/LMPA standard parts for the tensile tests; (b) Tensile machine setup; (c) Broken parts after the tensile tests; (d, e, f) Stress–strain curves of the PLA and PLA/LMPA parts subjected to tensile testing speeds of 1, 50, and 100 mm/min, respectively; (g) Results of the Young's modulus and tensile strength tests; (h) 3D printed PLA and PLA/LMPA standard parts for the three-point bending tests; (i) Three-point bending machine setup; (j) Broken parts after the three-point bending tests; (k, l, m) Load–displacement curves of the PLA and PLA/LMPA parts subjected to three-point bending test speeds of 1, 50, and 100 mm/min, respectively; (n) Flexural modulus and flexural strength values during the three-point bending tests. (PLA = polylactic acid; LMPA = low-melting-point alloy).

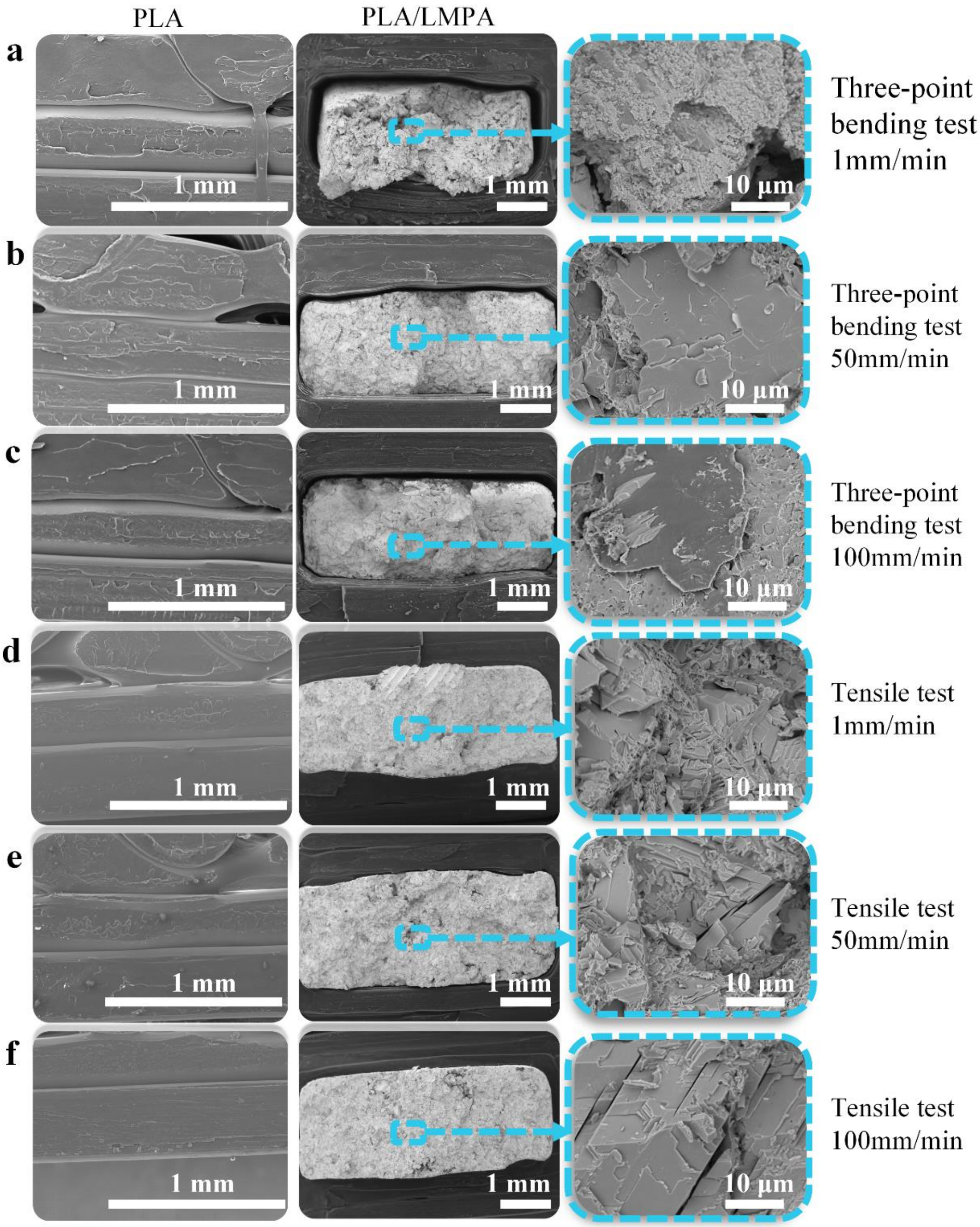

Figure 4. SEM images of the fractured surfaces of the PLA and PLA/LMPA test pieces after (a) the three-point bending test at 1 mm/min; (b) the three-point bending test at 50 mm/min; (c) the three-point bending test at 100 mm/min; (d) the tensile test at 1 mm/min; (e) the tensile test at 50 mm/min; and (f) the tensile test at 100 mm/min. (SEM = scanning electron microscopy; PLA = polylactic acid; LMPA = low-melting-point alloy).

2.3 3D printed products with internal electrical wires produced without an assembly step

To demonstrate the fabrication of 3D products featuring LMPAs that act as internal electrical wires, we designed two test pieces: a test piece comprising the letters CUHK; and a test piece comprising a “spring light” (i.e., an LED attached to a plastic spring with an internally printed LMPA that acts as an electrical wire). These two test pieces were designed using Autodesk Inventor Professional 2020, and are illustrated in Figure 5(a), (b), (e), and (f). Each hole or through-hole was 1.5 mm in diameter, and was filled with the LMPA during 3D printing. The dimensions of the CUHK piece were 196 × 66 × 35 mm. As shown in the figure, the CUHK piece was successfully fabricated with internal electrical wires comprising the LMPA without the necessity of an assembly step. Figure 5(c) shows the final printed CUHK piece, and Figure 5(d) shows the piece with the LEDs on. Figure 5(e) and (f) show the 3D spring light piece. Figure 5(g) shows the printed spring light piece, and Figure 5(h) shows the piece with the LED on. The CUHK and spring light pieces are shown herein as examples. However, other 3D applications/products that require internal electrical wires can be designed and fabricated using the proposed method. This reduces the postprocessing cost. Moreover, the technique can be used to produce complex 3D electrical parts that would have been impossible to make using traditional manufacturing methods.

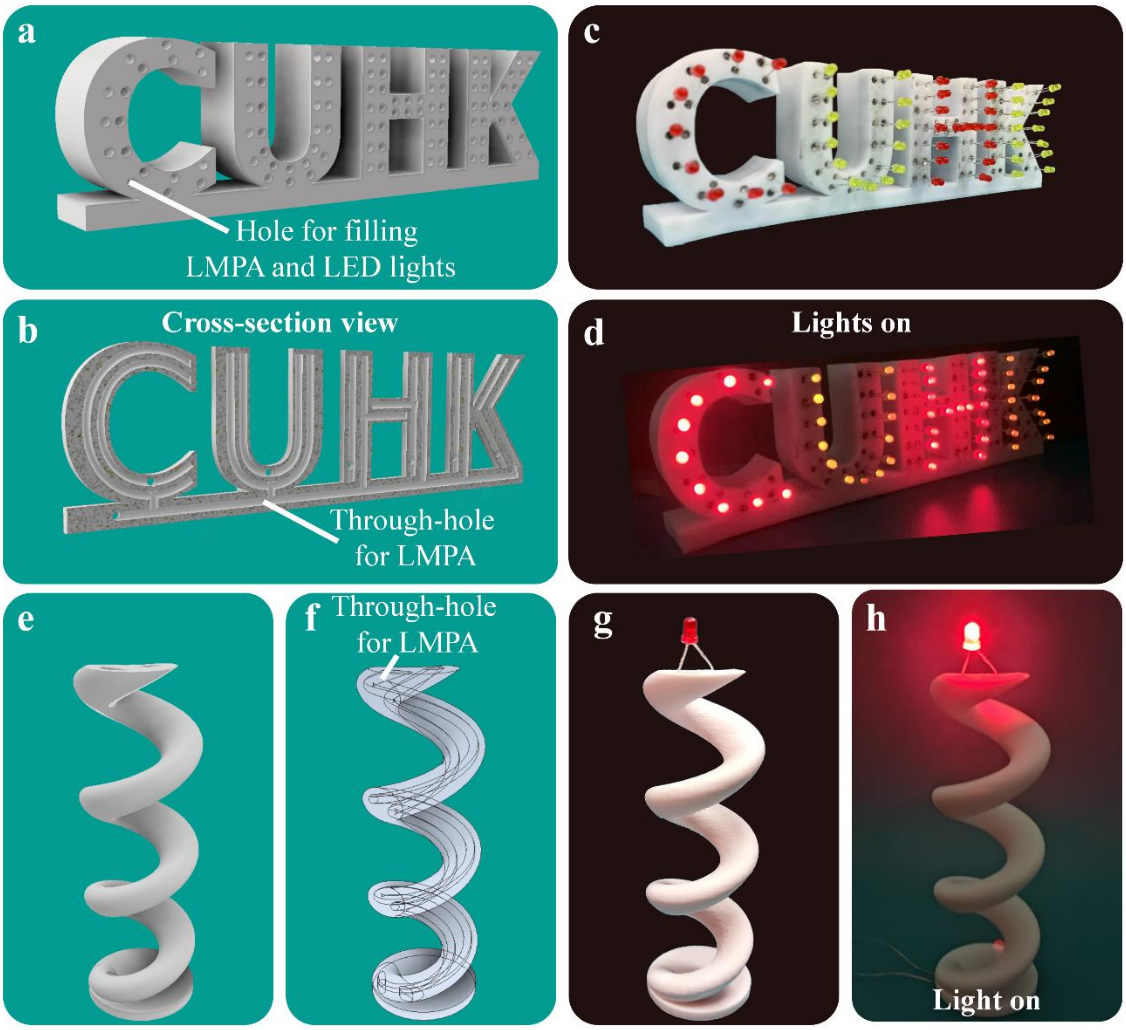

Figure 5. (a, b) Designed CUHK piece and its cross-section view; (c) Fabricated CUHK piece; (d) Fabricated CUHK piece with LED lights turned on; (e, f) Designed 3D spring light piece and its transparent view; (g) Fabricated spring light piece; (h) Fabricated spring light piece with LED light turned on. (LED = light-emitting diode; LMPA = low-melting-point alloy).

3. Conclusion

The present paper proposes a novel strategy for 3D printing LMPA parts, including LMPA/polymer composite parts and complex pure LMPA parts. The strategy can be used to fabricate integrated LMPA polymer parts with improved mechanical properties, fabricate complex pure LMPA parts, and fabricate complex parts with electrical functions without the need for post-assembly. Therefore, we designed and 3D printed standard parts for tensile and three-point bending tests. The results revealed that the integrated LMPA parts had much better mechanical performances than those produced conventionally. As shown previously, the proposed strategy was also used to 3D print complex pure LMPA parts. We successfully 3D printed various lattice, bone, and tooth structures. To the best of our knowledge, the present study is the first to demonstrate the fabrication of complex LMPA structures using EAM. The ability to 3D print complex LMPA parts provides greater freedom for the design of LMPA structures, which are potentially useful in various fields including electromagnetic shielding, biomedicine, thermal management, and energy harvesting. Ultimately, we demonstrated the 3D printing of whole products with electrical functions without the necessity of assembly (using CUHK and spring light test pieces). This would reduce the postprocessing cost and could be used to produce complex 3D electrical parts that are impossible to fabricate using traditional manufacturing techniques. Various other materials and applications could be realized in addition to applying the proposed strategy to LMPAs. For example, the proposed strategy could be used to 3D print a wax statue, whereby wax is used instead of LMPA, and poly(vinyl alcohol) (PVA) is used instead of PLA. PVA can be dissolved in water and wax is commonly used in the fabrication of statues. The statue model could be used as the original model, and after reversing the statue model, the reversed part could be used for 3D printing and wax filling. Moreover, other types of LMPA with different elements could also be used.

4. Experimental Section

4.1 Materials

The PLA was from Polymaker Ltd. The PLA filament was 1.75 mm in diameter. The LMPA was from Wude Alloys Ltd, China, and consisted of Sn 12.5%, Bi 50%, Pb 25%, and Cd 12.5% (the solid and liquid LMPA and its element mapping are shown in Figure S1). The melting point of this LMPA was 70°C. The dichloromethane (batch number 22020141) used to dissolve the PLA was from RCI Labscan Ltd, Thailand.

4.2 Mechanical testing

A CMT5105 universal electromechanical testing machine from MTS Systems Co., Ltd, China with 2 kN load cell was used for the tensile and three-point bending tests. Standard test pieces were designed for these tests. Details of their design are provided in the subsequent section. The tensile tests were conducted at various speeds, i.e., 1, 50, and 100 mm/min. The bending load velocities applied in the three-point bending tests were 1, 50, and 100 mm/min. Three tests were performed for each design.

4.3 Working principle of the customized 3D printer

The 3D printer used in the present study was originally from Polarbear 3D, and was customized by the authors. The basic principle is similar to that operating in traditional FDM. As shown in Figure S2, nozzle 1 was the same as a traditional nozzle; we added a second nozzle (nozzle 2) for LMPA extrusion. The printing process can be divided into two stages. The first stage resembles conventional 3D printing, and involves the layer-by-layer fabrication of a reversed

3D part from the bottom to the top. In the second stage, nozzle 1 is closed, and nozzle 2 injects the LMPA into the interior of the reversed 3D part. Nozzle 2 comprises a syringe pump with a heating function. The syringe pump was designed as shown in Figure S3(a). The working principle of the pump is as follows. Initially, the pump is full of LMPA. The heater is used to heat the LMPA to a specific temperature (above the melting temperature of the LMPA), and the piston then moves down to inject a specific volume of the LMPA. As shown in Figure S3(a), if the diameter of the pump is *D*, the volume of the injected LMPA (*V*) can be calculated using Equation 1:

$$V = z\pi(\frac{D}{2})^2, \tag{1}$$

where *z* is the squeezed height of the piston. Taking the TPMS structure shown in Figure S3(b) as an example, the volume of LMPA required can be calculated and then substituted into Equation 1 to determine the squeezed height *z*.

4.4 3D printing settings

The key PLA printing parameters were set as follows: print temperature, 205°C; print speed, 60 mm/s; layer height, 0.15 mm; infill density, 20%; and bed temperature, 45°C. When printing LMPA, the printing temperature was set at 100°C, and the print bed and chamber temperatures were set at 70°C.

4.5 SEM and X-ray fluorescence spectroscopy (EDX) analysis

The cross-sectional morphologies of the parts after the tensile and three-point bending tests were investigated using a TM3030Plus SEM microscope (Hitachi) at an accelerating voltage of 15 kV and a vacuum of 45 Pa. The element mapping of the LMPA was acquired using a XFlash660 energy-dispersive EDX detector (Bruker, Germany).

4.6 Electrical testing

An MS-305D direct current system (MAISHENG) was used to supply power to the printed CUHK and spring lights at 3 V.

4.7 Design of the CUHK test piece

The CUHK test piece with internal electrical wires was designed using Autodesk Inventor Professional 2020, and is illustrated in Figure S4. Each hole and through-hole had a diameter of 1.5 mm. The dimensions of the whole test piece were 196 × 66 × 35 mm.

4.8 Design of the pure LMPA structures

Herein, we present two kinds of structures: TPMS-based structures and lattice structures. Both are considered natural fundamental building blocks.

4.8.1 Design of TPMS-based porous structures

Most natural porous structures have nonuniform and irregular pores. Biomimetic structures are similar to porous biological structures. They can be generated by controlling the distribution of periodic parameters and curvature parameters based on the implicit surface characteristics of a TPMS. A TPMS-based porous structure can be described by the intersection of two solids that are defined by two signed distance fields ϕ_1 and ϕ_2:

$$\begin{aligned} \phi_1 &= \varphi + C, \\ \phi_2 &= C - \varphi, \\ \phi_s &= \min(\phi_1, \phi_2), \end{aligned} \tag{2}$$

where ϕ_1 and ϕ_2 represent two signed distance fields determined by the TPMS function φ, and C is the physical offset, which measures the algebraic distance between two surfaces $\phi_i = 0$ ($i = 1$ or 2) and $\varphi = 0$. The porous structure is defined by $\phi_s > 0$, which is the intersection of two solids $\phi_1 > 0$ and $\phi_2 > 0$. Figure S5 (a) shows details of the geometric representation. ϕ can be generated from the Fourier series on the periodic nodal surface.[33] The representations can be stated as follows:

$$\varphi(\mathbf{r}) = \sum_{k=1}^{K} A_k \cos\left[\frac{2\pi(\mathbf{h}_k \cdot \mathbf{r})}{\lambda_k} + P_k\right] = M, \tag{3}$$

in which $\mathrm{r} = (x, y, z) \in \mathbb{R}^3$ is a location vector, A_k is the amplitude, h_k is the k-th lattice vector, λ_k is the period factor, P_k is the function phase, and M is a constant. The topology of the TPMS can be satisfactorily reproduced by truncating the series to the maximum term, giving the following nodal approximation of a gyroid surface:

$$\begin{aligned}\varphi_G(\mathbf{r}) = \quad & \sin(2\pi t_x x)\cos(2\pi t_y y) + \sin(2\pi t_z z)\cos(2\pi t_x x) \\ & + \sin(2\pi t_y y)\cos(2\pi t_z z) = M,\end{aligned} \tag{4}$$

where t_x, t_y, and t_z represent periodic parameters along the x-, y-, and z-axes, respectively, and M is a nonzero constant.

The TPMS-based porous filling of a given model Ω_{Model} is formulated as:

$$\phi_{Final} = \min(\phi_s, \phi_{Model}), \tag{5}$$

where ϕ_{Model} is the signed distance field of the shape of model Ω_{Model}. In the present study, we randomly generated t_x, t_y, and t_z to achieve a porous entity filled with nonuniform three-period minimal surfaces. Figure S5 (d)-(f) show porous filling of the nonuniform minimal surfaces in the 3D entities.

4.8.2 Design of the lattice structures

Lattice structures are becoming increasingly common in product design because they have high stiffness-to-weight ratios. We adopted common lattice types (Honeycomb, X, Cross, Tesseract, Octet, and Star) to generate the volume lattice structures, as shown in Figure S6.

4.8.3 Design of the reversed 3D printing part

We designed a porous structure model Ω_{porous}, and calculated its bounding box B_{porous}. The reversed 3D printing part was obtained from B_{porous}. The design pipeline and the reversed 3D lattice structures of the printing parts are shown in Figure S7.

4.9 Design of parts for mechanical testing

We determined the sizes of the tensile test pieces according to ISO 527–1:2019[34] and ISO 527–2:2012,[35] as shown in Figure S8(a) and (b), and determined the sizes of the three-point bending test pieces according to ISO 178:2019,[36] as shown in Figure S8(c) and (d). Both tensile and three-point bending tests were carried out three times on each design (three parts printed for each design). The printing direction is shown in Figure S9. PLA was used as the polymer material, and LMPA consisting of Sn 12.5%, Bi 50%, Pb 25%, and Cd 12.5% was used for the filling. The print parameters were as follows: print temperature, 205°C; print speed, 60 mm/s; layer height, 0.15 mm; bed temperature, 45°C; and infill density, 20%. The printing temperature for LMPA was set at 100°C, and the print bed temperature was set at 70°C.

Acknowledgements

We thank Frank Kitching, MSc., from Edanz (www.edanz.com/ac) for editing a draft of this manuscript. We would also like to thank Mr. Allan Mok for his assistance in the experiments, Xuewen Gong for her suggestions on figure drafting, and Nan Zheng for her help on lattice structure design. This study is funded by Research Grants Council (CUHK 14210019), Innovation and Technology Commission (MHP/043/20, under PiH/278/22), Hong Kong Special Administrative Region, China, Provincial Natural Science Foundation of Anhui (2208085QA01), and Fundamental Research Funds for the Central Universities (WK0010000075).

References

[1] I. Gibson, D. W. Rosen, B. Stucker, M. Khorasani, *Additive Manufacturing Technologies, Third Edition, Springer*, **2021**.

[2] T. Wohlers, T. Gornet, *Wohlers Rep. 2014 - 3D Print. Addit. Manuf. State Ind.* **2014**.

[3] H. Cui, D. Yao, R. Hensleigh, H. Lu, A. Calderon, Z. Xu, S. Davaria, Z. Wang, P. Mercier, P. Tarazaga, X. Zheng, *Science.* **2022**, *376*, 1287.

[4] B. E. Kelly, I. Bhattacharya, H. Heidari, M. Shusteff, C. M. Spadaccini, H. K. Taylor, *Science.* **2019**, *363*, 1075.

[5] Y. Zhang, L. Wu, M. Zou, L. Zhang, Y. Song, *Adv. Mater.* **2022**, *34*, 2107249.

[6] Z. C. Eckel, C. Zhou, J. H. Martin, A. J. Jacobsen, W. B. Carter, T. A. Schaedler, *Science.* **2016**, *351*, 58.

[7] M. Layani, X. Wang, S. Magdassi, M. Layani, X. Wang, S. Magdassi, *Adv. Mater.* **2018**, *30*, 1706344.

[8] H. Wang, L. Y. Liu, P. Ye, Z. Huang, A. Y. R. Ng, Z. Du, Z. Dong, D. Tang, C. L. Gan, *Adv. Mater.* **2021**, *33*, 2007072.

[9] K. Zhang, P. Chermprayong, F. Xiao, D. Tzoumanikas, B. Dams, S. Kay, B. B. Kocer, A. Burns, L. Orr, C. Choi, D. D. Darekar, W. Li, S. Hirschmann, V. Soana, S. A. Ngah, S. Sareh, A. Choubey, L. Margheri, V. M. Pawar, R. J. Ball, C. Williams, P. Shepherd, S. Leutenegger, R. Stuart-Smith, M. Kovac, *Nat.* **2022**, *609*, 709.

[10] J. H. Martin, B. D. Yahata, J. M. Hundley, J. A. Mayer, T. A. Schaedler, T. M. Pollock, *Nat.* **2017**, *549*, 365.

[11] D. Zhang, D. Qiu, M. A. Gibson, Y. Zheng, H. L. Fraser, D. H. StJohn, M. A. Easton, *Nat.* **2019**, *576*, 91.

[12] J. Ren, Y. Zhang, D. Zhao, Y. Chen, S. Guan, Y. Liu, L. Liu, S. Peng, F. Kong, J. D. Poplawsky, G. Gao, T. Voisin, K. An, Y. M. Wang, K. Y. Xie, T. Zhu, W. Chen, *Nat.* **2022**, *608*, 62.

[13] P. Kürnsteiner, M. B. Wilms, A. Weisheit, B. Gault, E. A. Jägle, D. Raabe, *Nat.* **2020**, *582*, 515.

[14] A. Behroozfar, S. Daryadel, S. R. Morsali, S. Moreno, M. Baniasadi, R. A. Bernal, M. Minary-Jolandan, *Adv. Mater.* **2018**, *30*, 1705107.

[15] F. Kotz, K. Arnold, W. Bauer, D. Schild, N. Keller, K. Sachsenheimer, T. M. Nargang, C. Richter, D. Helmer, B. E. Rapp, *Nat.* **2017**, *544*, 337.

[16] Y. Liu, K. N. Tu, *Mater. Today Adv.* **2020**, *8*, 100115.

[17] T. Daeneke, K. Khoshmanesh, N. Mahmood, I. A. De Castro, D. Esrafilzadeh, S. J. Barrow, M. D. Dickey, K. Kalantar-Zadeh, *Chem. Soc. Rev.* **2018**, *47*, 4073.

[18] J. Zhang, Y. Yao, L. Sheng, J. Liu, *Adv. Mater.* **2015**, *27*, 2648.

[19] X. Wang, R. Guo, J. Liu, *Adv. Mater. Technol.* **2019**, *4*, 1800549.

[20] X. D. Zhang, X. H. Yang, Y. X. Zhou, W. Rao, J. Y. Gao, Y. J. Ding, Q. Q. Shu, J. Liu, *Energy Convers. Manag.* **2019**, *185*, 248.

[21] X. H. Yang, S. C. Tan, Z. Z. He, J. Liu, *Energy Convers. Manag.* **2018**, *160*, 467.

[22] S. Xu, X. H. Yang, S. S. Tang, J. Liu, *Int. J. Hydrogen Energy* **2019**, *44*, 17505.

[23] M. Zhang, P. Zhang, C. Zhang, Y. Wang, H. Chang, W. Rao, *Appl. Mater. Today* **2020**, *19*, 100612.

[24] J. Yan, Y. Lu, G. Chen, M. Yang, Z. Gu, *Chem. Soc. Rev.* **2018**, *47*, 2518.

[25] Y. Huang, Y. Cao, H. Qin, *Adv. Eng. Mater.* **2022**, *24*, 2200091.

[26] N. Warrier, K. H. Kate, *Prog. Addit. Manuf.* **2018**, *3*, 51.

[27] P. C. Hsieh, C. H. Tsai, B. H. Liu, W. C. J. Wei, A. B. Wang, R. C. Luo, *Proc. IEEE Int. Conf. Ind. Technol.* **2016**, *2016-May*, 1138.

[28] J. Yang, K. Y. Kwon, S. Kanetkar, R. Xing, P. Nithyanandam, Y. Li, W. Jung, W. Gong, M. Tuman, Q. Shen, M. Wang, T. Ghosh, K. Chatterjee, X. Wang, D. Zhang, T. il Kim, V. K. Truong, M. D. Dickey, *Adv. Mater. Technol.* **2022**, *7*, 2101074.

[29] W. Lee, H. Kim, I. Kang, H. Park, J. Jung, H. Lee, H. Park, J. S. Park, J. M. Yuk, S. Ryu, J.-W. Jeong, J. Kang, *Science.* **2022**, *378*, 637.

[30] C. Okutani, T. Yokota, H. Miyazako, T. Someya, *Adv. Mater. Technol.* **2022**, *7*, 2101657.

[31] J. Y. Gao, S. Chen, T. Y. Liu, J. Ye, J. Liu, *Mater. Today* **2021**, *49*, 201.

[32] F. Deng, Q. K. Nguyen, P. Zhang, *Addit. Manuf.* **2020**, *33*, 101117.

[33] P. J. F. Gandy, S. Bardhan, A. L. Mackay, J. Klinowski, *Chem. Phys. Lett.* **2001**, *336*, 187.

[34] ISO527-1:2019, *Plastics—Determination of Tensile Properties—Part 1: General Principles. Geneva, Switzerland: International Organization for Standardization*, **2012**.

[35] ISO527-2:2012, *Plastics—Determination of Tensile Properties—Part 2: Test Conditions for Moulding and Extrusion Plastics. Geneva, Switzerland: International Organization for Standardization*, **2012**.

[36] ISO 178:2019, *Plastics—Determination of Flexural Properties. Geneva, Switzerland: International Organization for Standardization*, **2012**.

Supporting Information

Supplementary information for

Low-melting-point alloys integrated extrusion additive manufacturing

Jingchao Jiang, Xiaoya Zhai, Kang Zhang, Liuchao Jin, Qitao Lu, Zhichao Shen, Wei-Hsin Liao*

*Correspondence to: whliao@cuhk.edu.hk

This file includes:

Figures S1 to S9
Captions for Movies S1 to S4

Other supplementary information:

Movies S1 to S4

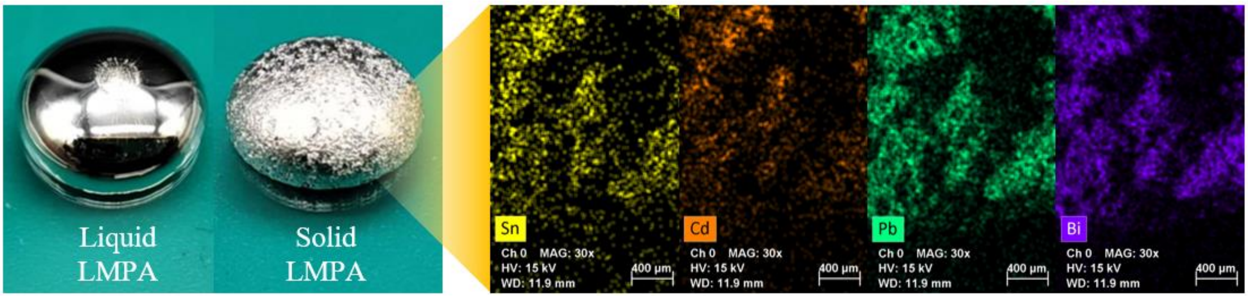

Figure S1.
Images of the liquid and solid LMPA and its element mapping. (LMPA = low-melting-point alloy).

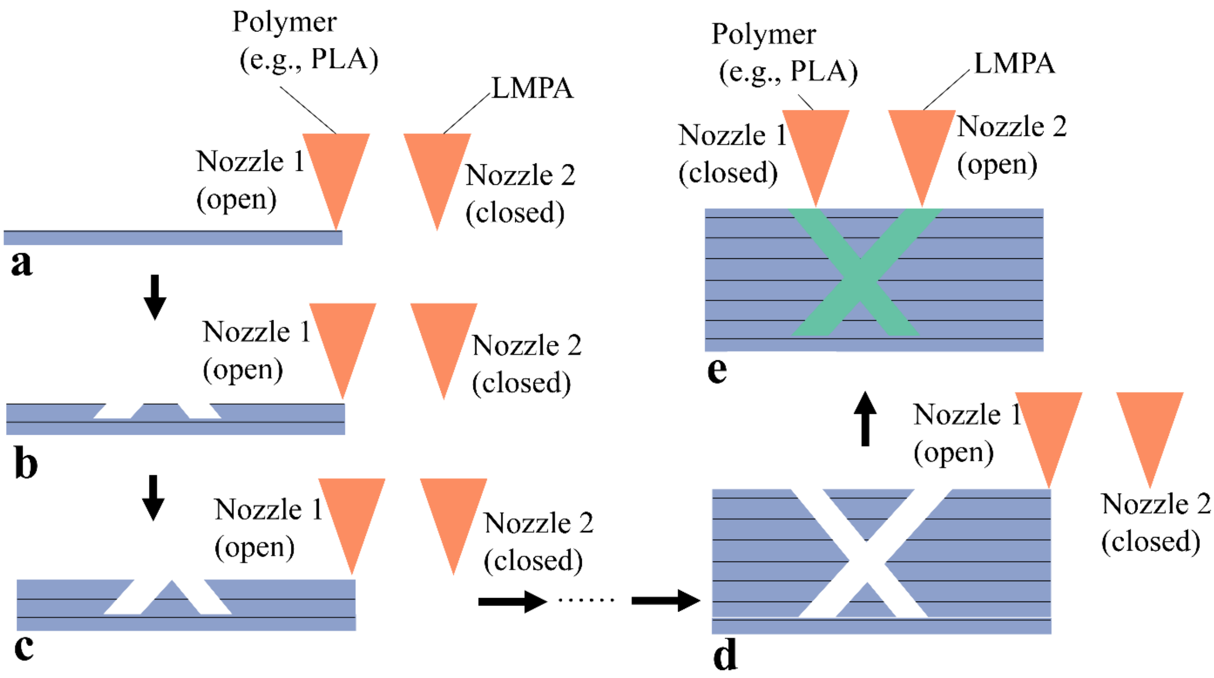

Figure S2.

Illustration of the printing process. (a)–(d) 3D printing polymer for the reversed 3D model; (e) The LMPA injection process. (PLA = polylactic acid; LMPA = low-melting-point alloy).

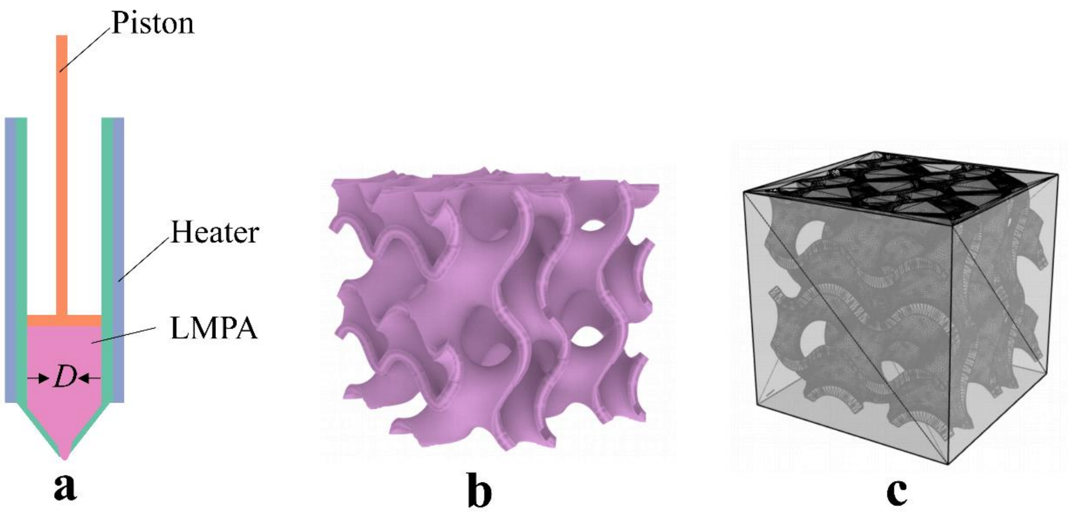

Figure S3.

Illustration showing the design of the syringe pump. (a) The syringe pump; (b) The TPMS structure; (c) The reversed TPMS test piece for 3D printing. (TPMS = triply periodic minimal surface).

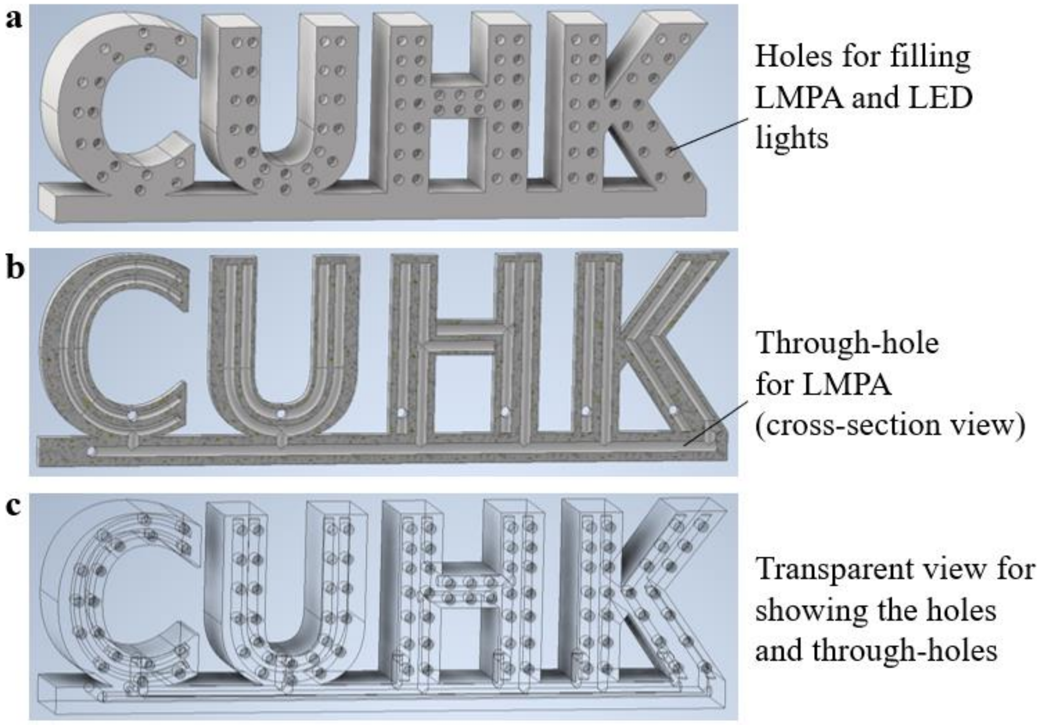

Figure S4.

CUHK test piece with holes and through-holes for filling LMPA, designed for whole product fabrication without the necessity of assembling electrical wires. (a) Illustration of the holes; (b) Cross-sectional view of the through-holes; (c) Transparent view. (CUHK = Chinese University of Hong Kong; LMPA = low-melting-point alloy).

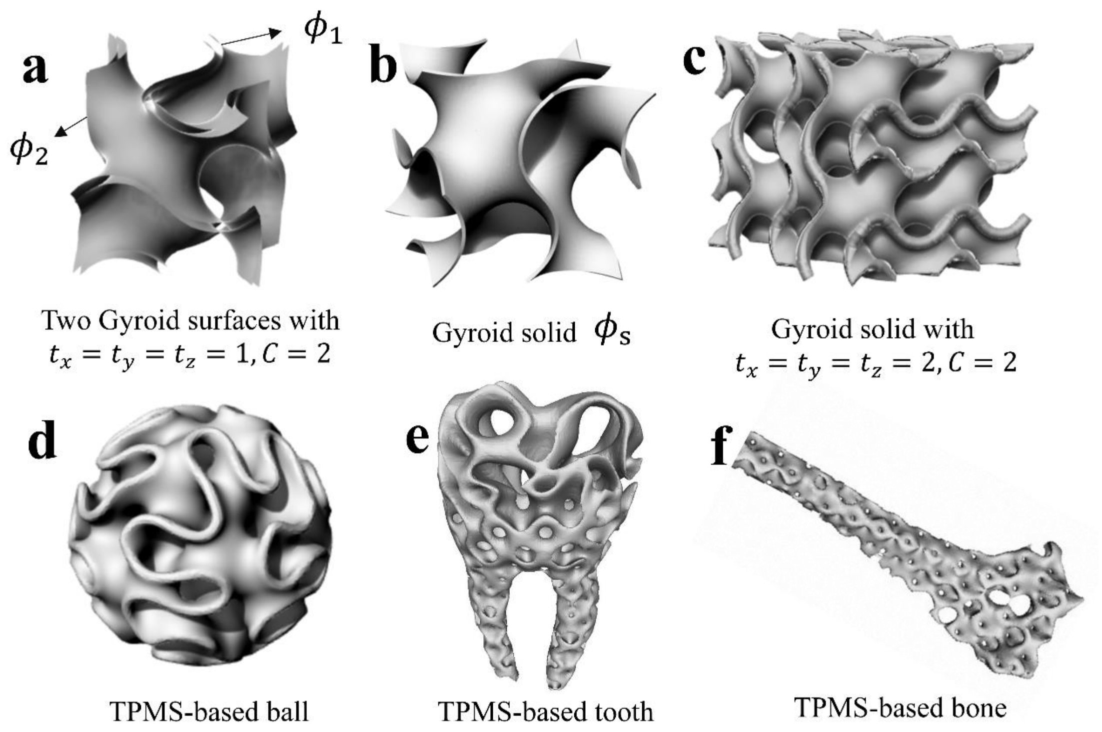

Figure S5.

(a)-(c) Illustration of the geometric representation of a TPMS-based porous structure; (d) TPMS-based ball; (e) TPMS-based tooth; (f) TPMS-based bone. (TPMS = triply periodic minimal surface).

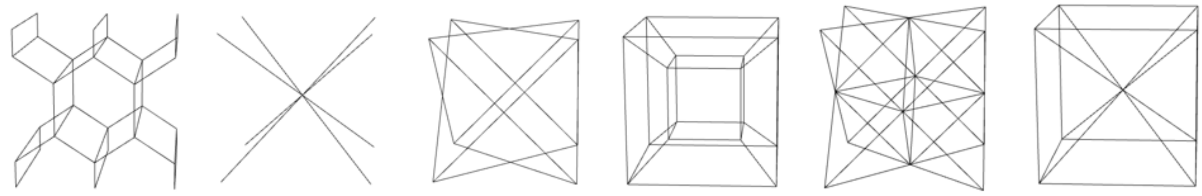

Figure S6.
Illustration of the various lattice structures (Honeycomb, X, Cross, Tesseract, Octet, and Star).

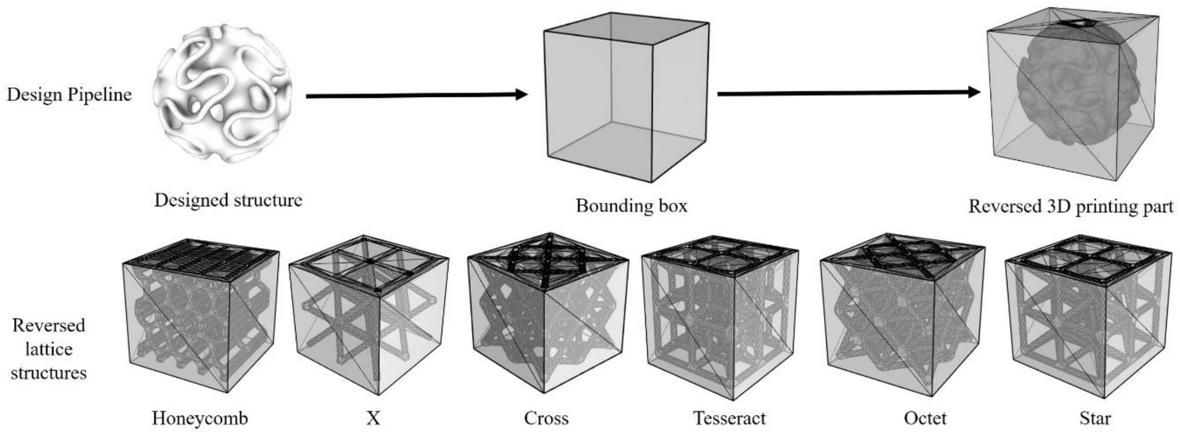

Figure S7.
Pipeline for obtaining the reversed 3D printing parts.

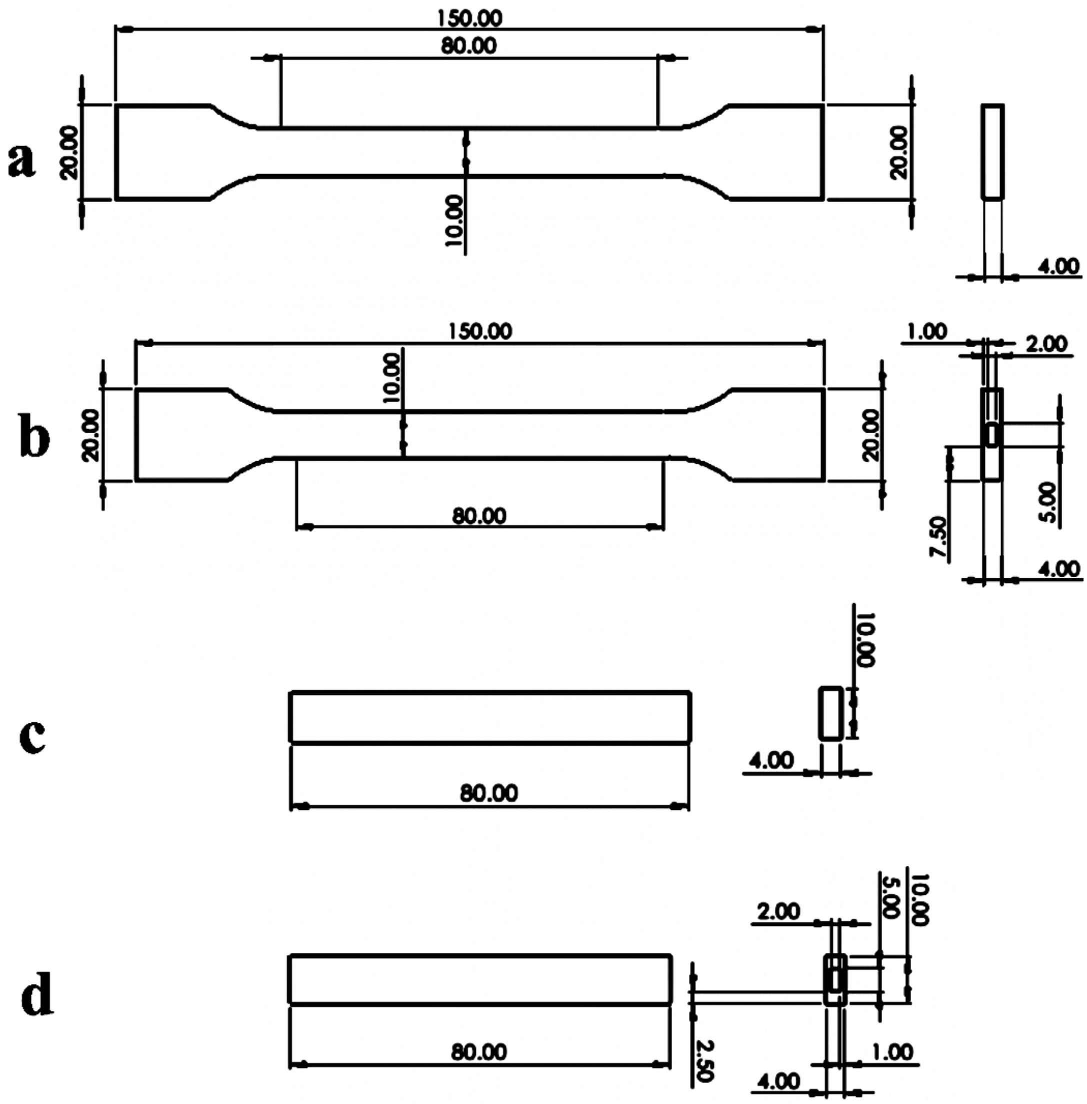

Figure S8.

Test pieces designed for the tensile tests: (a) pure PLA and (b) LMPA/PLA composite; and test pieces designed for the three-point bending tests: (c) pure PLA and (d) LMPA/PLA composite (unit: mm). (PLA = polylactic acid; LMPA = low-melting-point alloy).

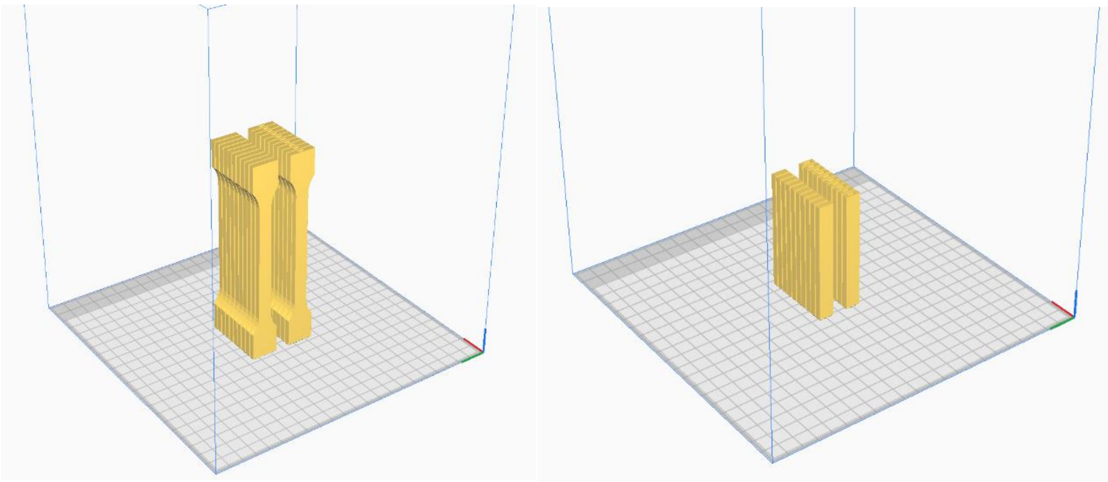

Figure S9.
Printing direction used to produce the test pieces for the tensile and three-point bending tests.

Captions for Movies S1 to S4.

Movie S1
Three-point bending tests on the PLA and PLA/LMPA test pieces subjected to various testing conditions (testing speeds of 1, 50, and 100 mm/min). (LMPA = low-melting-point alloy; PLA = polylactic acid).

Movie S2
Tensile tests on the PLA and PLA/LMPA test pieces subjected to various testing conditions (testing speeds of 1, 50, and 100 mm/min). (LMPA = low-melting-point alloy; PLA = polylactic acid).

Movie S3
Demonstration of the CUHK (Chinese University of Hong Kong) and light spring test pieces.

Movie S4
Demonstration of the whole 3D printing process used to obtain complex pure LMPA structures. (LMPA = low-melting-point alloy).